JOURNAL OF PROPULSION AND POWER
Vol. 13, No. 6, November–December 1997

Study of a Supersonic Combustor Employing Swept Ramp Fuel Injectors

Dean R. Eklund*
Royal Institute of Technology, Stockholm S-100 44, Sweden
Scott D. Stouffer†
Virginia Polytechnic Institute and State University, Blacksburg, Virginia 24061
and
G. Burton Northam‡
NASA Langley Research Center, Hampton, Virginia 23681

A computational study of a scramjet combustor with swept ramp fuel injectors was conducted with the SPARK Navier–Stokes computer code. Turbulence was modeled with a two-zone algebraic turbulence model, while combustion was modeled with two finite rate H_2–air chemistry models. The calculated reacting flowfield was mixing-limited. However, the extent of mixing was affected by the chemical reactions. Heat release from the chemical reactions significantly reduced the mixing between the fuel and airstreams. Comparisons between the calculations and experimental measurements of the wall pressure, surface heat flux, in-stream pitot pressure, as well as Mie scattering flow visualization were made and good overall agreement was observed.

Nomenclature

$A_j T^{b_j}$	=	Arrhenius pre-exponential factor for the jth reaction
c_{μ_T}	=	eddy viscosity constant
D	=	Damkohler number
F	=	force
G	=	gap, equals twice the duct height, 7.62 cm
k_{f_j}	=	reaction rate coefficient for the jth reaction
M	=	Mach number
p	=	pressure
T	=	temperature
T_{a_j}	=	activation temperature for the jth reaction
u	=	velocity component in the x direction
$\hat{V}_i$	=	diffusion velocity of species i in the x direction
$\dot{w}_i$	=	chemical production rate of species i
x, y, z	=	Cartesian coordinates
$Y^P_{H_2O}$	=	mass fraction of water caused by combustion
Z^I_H	=	mass fraction of elemental hydrogen originating in the fuel jet
Δt	=	time step
ρ_i	=	density of species i

Introduction

ENHANCED mixing, and thus reduced combustor length, is an important factor in the design of supersonic combustion ramjet (scramjet) engines. A number of experimental, theoretical, and computational studies are being conducted to explore techniques to enhance mixing and combustion in supersonic and hypersonic reacting flows. Ramp fuel injectors are advantageous, in part, because they provide for nearly parallel injection of the fuel. Parallel injection is useful at high speeds to extract additional thrust from regeneratively heated fuel that has been used as a coolant for the vehicle and engine. Techniques are being investigated to enhance the relatively slow mixing usually associated with parallel injection.

Examples of mixing concepts being investigated include low-angle injection,[1] swirling fuel jets,[2] nonaxisymmetric internal fuel injection nozzle geometries,[3,4] tabs inside fuel injection nozzles,[5] shock interactions with the fuel jet,[6] and ramp injectors.[7–13] Earlier direct-connect scramjet tests at NASA Langley Research Center with swept compression ramps were conducted at Mach 2.0 and 3.0 inflow test conditions.[7] The results suggested that rapid mixing and combustion, approaching the performance of transverse injectors, could be accomplished while maintaining nearly parallel injection with respect to the oncoming stream. In these previous tests, the combustor model used two fuel-injector ramps. Later tests were conducted with four wall-mounted ramp injectors, to partially eliminate side wall effects. The four-ramp injector configuration has been tested in a direct-connect vitiated heater facility at the following inlet conditions: T_0 = 1944 K, P = 1 atm, and M = 2.7. The results of the experimental tests, which included wall pressures, heat fluxes, Mie scattering flow visualization, and pitot pressure surveys, are presented in Ref. 12.

This paper presents calculations of the reacting flow through a supersonic combustor employing swept ramp fuel injectors. Numerical issues of accuracy and efficiency are addressed, features of the reacting flow are examined, and detailed comparisons between the Navier–Stokes calculations and the experimental measurements are made.

Experimental Technique

Injector Design

The injector block that was used in this investigation consisted of four swept ramp fuel injectors. The ramp angle and the sweep angle were both 10.3 deg. Four Mach 1.7 fuel injection nozzles angled at 10 deg with respect to the main flow

Received Aug. 31, 1995; revision received July 10, 1997; accepted for publication July 12, 1997.

*Lecturer, Chair of Heat and Power Technology. Senior Member AIAA.

†Graduate Student, Mechanical Engineering Department; currently Associate Research Engineer, University of Dayton, Research Institute, Dayton, OH. Member AIAA.

‡Senior Research Engineer, Hypersonic Propulsion Branch; currently Senior Research Scientist, Environmental Interactions Branch. Senior Member AIAA.

Table 1 Inflow conditions

Parameter	Vitiated stream	Injector
Static pressure, kPa	104	222
Static temperature, K	932	190
Velocity, m/s	1710	1781
Mach number	2.7	1.7
H_2 mass fraction	0.164E−5	1
O_2 mass fraction	0.256E0	0
H_2O mass fraction	0.191E0	0
OH mass fraction	0.704E−3	0
H mass fraction	0.365E−7	0
O mass fraction	0.223E−4	0
N_2 mass fraction	0.552E0	0
Mass flow rate, g/s	460	10.9

Table 2 Experimental uncertainty

Measurement	Uncertainty
Static pressure	±4.1 kPa
Pitot pressure	±8.8 kPa
Surface heat flux	±5.8%

were used. The injection nozzles were conical shaped with an 8-deg half-angle, and an exit diameter of 0.71 cm. The duct height at the entrance of the combustor, upstream of the ramps, was 3.81 cm or 0.5G. The dimensions of the ramp base were 1.52 cm wide by 1.27 cm high, creating a blockage of 12% of the combustor area.

The combustor had a short (0.92G) constant area section downstream of the injector, followed by 2.15-deg divergent top and bottom combustor walls that extended from x/G = 0.92 to 15.4. The combustor was attached to a 22-deg divergent nozzle connected to a vacuum exhaust system. The combustor walls were uncooled and the run times were limited to 10 s to avoid excessive wall temperatures.

The tests were conducted in the NASA Langley Research Center's Direct-Connect Supersonic Combustor Test Facility. In the tests, the flow from a scramjet inlet was simulated by the facility nozzle. High-enthalpy air was provided by a hydrogen–air vitiated heater with oxygen replenishment to 21% by volume. The hydrogen–oxygen–air burner exhausted through a water-cooled Mach 2.7 nozzle. The flow conditions for the cases considered in this study are listed in Table 1.

Measurements

Wall pressures were measured at over 200 locations along the combustor. Wall heat fluxes along the combustor walls were obtained by direct measurement with Gardon gauges and by calculation from time-dependent measurements of the inner wall surface temperature. A tungsten pitot probe was used to measure the pitot pressure distribution at the exit of the combustor. The experimental uncertainty for the measurements are listed in Table 2. Analysis of the uncertainty is given in Ref. 12. Also, Mie scattering from silica particles, generated by silane that was added to the hydrogen fuel, was used to visualize the penetration of reacted fuel across the combustor. Silane (SiH_4), a pyrophoric gas, reacts when it encounters air, forming small solid silica particles as a product. If the local conditions in the combustor are mixing-limited, then hydrogen–air reactions are not significantly altered by the presence of the silane; thus the silica particles generated may be used to provide visualization of the location of the products of the hydrogen–air reactions. The images that were acquired during the test qualitatively represent the average penetration of the reacted products across the combustor duct.

Numerical Technique

Computer Code

The low memory version of the three-dimensional SPARK Navier–Stokes code developed at the NASA Langley Research Center was used in this study. Details of the computer code are given in Refs. 14 and 15. The algorithm used in the calculations was the steady-state Cross–MacCormack algorithm developed by Carpenter.[15] The algorithm, while formally second-order accurate in space and time, attains fourth-order spatial accuracy at steady state. Fourth-order, second-difference artificial viscosity based on gradients of pressure and temperature is included in the solution algorithm to suppress numerical oscillations in the vicinity of shock waves and to enhance stability.

In a previous study,[16] relatively large errors in mass conservation were observed when employing a cold wall boundary condition. This phenomenon was investigated by making a series of two-dimensional calculations over a rearward-facing step. It was found that the contribution to the artificial viscosity from the gradients of temperature significantly impacts the mass conservation when there is a large thermal boundary layer as in the case of a cold wall. The conservation error resulted from high levels of numerical dissipation generated in the boundary layer throughout the computational domain. Hence, the coefficient of artificial viscosity associated with the gradients of temperature is required to be zero, or small when imposing a cold wall boundary condition.

Minor enhancements were made to the SPARK code to generalize the artificial viscosity and time-step calculations for curvilinear coordinates and to further reduce the memory requirements of the code. The enhancements are described in Ref. 13.

The turbulence model used in this study combines the Baldwin–Lomax model[17] along the walls with a mixing length model for the jets.[18] The constant in the mixing length model was c_{μ_t} = 0.00328, which is lower than the value originally recommended by Eggers,[18] based on a study of coaxial jets. The implementation of this model is described in detail in Ref. 19. The turbulent Schmidt and Prandtl numbers were set to constant values of 0.5 and 0.9, respectively, whereas the turbulent viscosity was limited to 1000 times the laminar viscosity.

Two chemistry models were used in this work. The first contains six reacting species: H_2, O_2, H_2O, OH, H, and O, plus an inert species N_2 that interact through a seven-step reaction mechanism.[20] The second model includes two additional species: HO_2 and H_2O_2. The eight reacting species interact through a 19-step mechanism.[21] The reactions together with the constants appearing in the Arrhenius expression for the forward rate coefficient k_{f_j}

$$k_{f_j} = A_j T^{b_j} \exp[(-T_{a_j})/T] \tag{1}$$

are listed Ref. 13. The chemical production terms are evaluated from the reaction rates and the chemical composition of the gas by using the law of mass action. The effect of turbulent fluctuations on the chemical production terms was not modeled.

Computational Domain and Grids

Characteristics of the computational domain are listed in Table 3. The domain was divided into two sections. The first

Table 3 Dimensions of the computational domain

Feature	Centimeters	Gaps
Gap	7.62	1.0
Distance between the injector and the expansion corner	6.99	0.92
Distance between the injector and the end of the first half of the combustor	47.7	6.26
Distance between the injector and the end of the second half of the combustor	117.5	15.4
Duct height (downstream of the step)	3.81	0.50
Duct width	2.12	0.28
Injector diameter	0.71	0.093

section extended in the streamwise direction from the beginning of the ramp ($x/G = -0.92$) to $x/G = 6.26$. The second half of the domain extended from $x/G = 6.26$ to 15.4. The Mach number in the exit plane of the first section exceeded 1.35 outside of the boundary layer for each of the solutions. Hence, dividing the domain should not significantly affect the solution.

In the spanwise direction, the computational domain extended from the centerline of one jet to the centerline of the adjacent interstice. The domain extended in the normal direction from the bottom wall to the top wall of the duct. The streamwise, spanwise, and normal directions were represented by the x, y, and z coordinates, respectively, and the origin of the coordinate system was located on the bottom wall of the jet centerline at the base of the ramp.

Figure 1 shows the initial portion of the grid used for the swept ramp calculations (only every other grid point is shown). The grids used in this work were generated externally to the SPARK code using the exponential stretching functions found in Ref. 22. The grids were also passed through an elliptic solver routine written by White[23] to smooth the grid distribution. The dimension of the grid for the first half of the domain was 163 × 39 × 75 (x, y, and z, respectively). Grid stretching in the streamwise direction was employed at either end of the ramp, at the beginning of the 2.15-deg divergence, and at the outflow boundary. In the spanwise direction, grid stretching was employed at both the jet and interstice centerlines and along the side of the ramp. Grid stretching was also employed in the normal direction along the top and bottom walls and along the top surface of the ramp. The minimum grid spacing in the normal direction downstream of the ramp varied from a maximum of 40 μm ($z^+ = 35$) at the base of the ramp to a minimum of 7.3 μm ($z^+ = 9$). The injector was modeled with 87 points that were distributed to approximate a circular cross section. The injector is represented by the white region in Fig. 1.

The dimensions of the grids used for the second half of the combustor ($6.26 \leq x/G \leq 15.4$) were 77 × 20 × 75 and 77 × 20 × 101. The grid spacing in the normal direction at the top and bottom walls varied from 14 μm at the inflow plane to 20 μm at the exit plane for the first grid, and equaled 1 μm along the full extent of the domain for the second grid. The corresponding values of z^+ were approximately 13.5 and 8.0 for the top and bottom walls for the first grid, and approximately 0.9 and 0.4, respectively, for the second grid.

Boundary Conditions

A solution of the vitiated airflow through the $M = 2.7$ facility nozzle and the constant area section separating the exit of the nozzle and ramp surface was obtained. Spline fits of the calculated profiles of the flow entering the combustor were used to specify the velocity, pressure, and temperature values at the inflow boundary of the combustor. The calculated thickness of the turbulent boundary layer at the entrance of the combustor was approximately 5.6 mm or 0.44 ramp heights. The chemical composition of the inflow was obtained from an equilibrium calculation at the stagnation conditions. The inflow conditions are summarized in Table 1. The inflow conditions for the second half of the combustor were obtained from a spline fit of the solution at the exit plane of the first half of the domain.

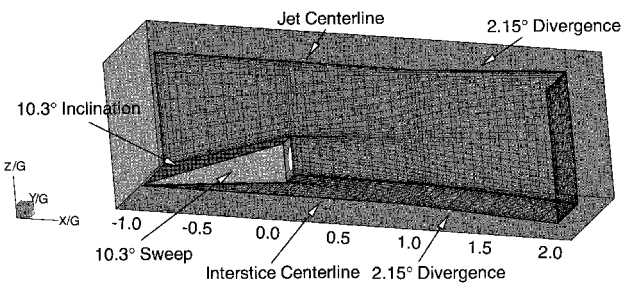

Fig. 1 Computational grid in the vicinity of the injector.

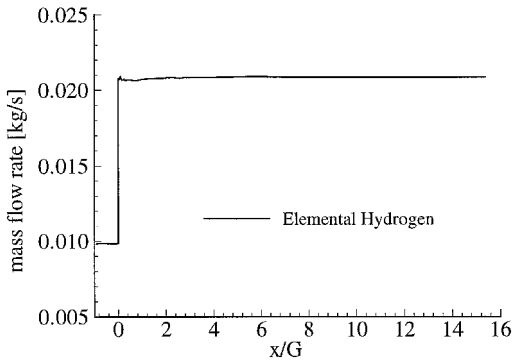

Fig. 2 Mass conservation of elemental hydrogen.

Symmetry boundary conditions were invoked at the two side planes (injector and interstice centerline planes). Along solid walls, the no slip-condition was imposed. Also, a zero normal pressure gradient and constant wall temperature was imposed. The wall temperature T_{Wall} was set equal to 670 K for the first half of the combustor. In the second half of the combustor, T_{Wall} was calculated from a linear fit of measured wall temperature values.

The jet issued from a conical nozzle and the trajectory of the jet was modeled as a point source. The points on the perimeter of the modeled injector were given a reduced velocity to match the prescribed mass flow rate. Finally, along the outflow boundary, the primitive variables were extrapolated using a first-order approximation.

Iteration Technique

The solutions were advanced in time using a local fluid time step calculated by combining the convective and the diffusive time scales. The Courant number was set equal to 0.5 for all of the calculations. The coefficient of artificial viscosity associated with pressure gradients was set between values of 0.5 and 1.0, whereas the coefficient of artificial viscosity associated with temperature gradients was set between values of 0.1 and 0.25. No ignition aids were introduced into the calculations.

A true steady-state solution was not attained for these flowfields. The residual, defined as the maximum change in the nondimensional density between successive iterations, typically dropped and then hovered at 10^{-3}. The maximum residual often was located in the recirculating flow region near the base of the injector. Convergence was assessed by inspection of the integrated values of the conserved variables, such as conservation of mass, as well as plots of mixing and chemical efficiency. Conservation of mass within 1% was attained. Figure 2 shows the mass conservation of elemental hydrogen for one of the reacting flowfield solutions (case 4). The nonreacting flow cases required approximately 10,000 iterations to achieve steady values for the integrated conserved quantities, while approximately 70,000 iterations were required to attain steady values for the integrated conserved quantities for the reacting flow cases.

Semi-Implicit and Explicit Chemistry

The species continuity equations that provide for the convection, diffusion, and production of each chemical species can be written for one coordinate direction as

$$\frac{\partial \boldsymbol{U}}{\partial t} + \frac{\partial \boldsymbol{E}}{\partial x} = \boldsymbol{H} \tag{2}$$

where

$$\boldsymbol{U} = \rho_i, \qquad \boldsymbol{E} = (\rho_i u + \rho_i \hat{V}_i), \qquad \boldsymbol{H} = \dot{w}_i \tag{3}$$

The chemical production terms appearing in the species continuity equations are typically associated with a wide range of time scales, which renders them mathematically stiff. The chemical production terms can be solved implicitly to counteract the stiffness. That is,

$$\boldsymbol{H}^{n+1} = \boldsymbol{H}^{n} + \frac{\partial \boldsymbol{H}^{n}}{\partial \boldsymbol{U}} \frac{\partial \boldsymbol{U}^{n}}{\partial t} \Delta t + \mathbb{O}(\Delta t^{2}) \tag{4}$$

which yields

$$\left(I - \frac{\partial \boldsymbol{H}^{n}}{\partial \boldsymbol{U}} \Delta t \right) \frac{\partial \boldsymbol{U}}{\partial t} + \frac{\partial \boldsymbol{E}}{\partial x} = \boldsymbol{H}^{n} \tag{5}$$

The preconditioning matrix $[I - (\partial \boldsymbol{H}/\partial \boldsymbol{U})^{n}\Delta t]$ can be represented conceptually by the scalar expression $1 - 1/D$, where D is defined as

$$D = \Delta t_{\text{Chem}}/\Delta t_{\text{Fluid}} \tag{6}$$

Here, Δt_{Fluid} is the fluid time scale obtained by combining the viscous and convective time constraints, and Δt_{Chem} is the smallest chemistry time scale, defined as

$$\Delta t_{\text{Chem}} = \min \left(\left| \frac{\partial \boldsymbol{H}^{n}}{\partial \boldsymbol{U}} \right|^{-1} \right) \tag{7}$$

Equation (7) was evaluated for one solution (case 4), and the Damkohler number was found to range between $1.E{-}1 < D < 1.E3$. Hence, the smallest chemical time scale was not significantly smaller than the fluid time scale and explicit solution of the chemistry, which does not require the inversion of a $n \times n$ matrix at each point of the domain (where n is the number of species equations that are solved) was employed. A time-step constraint was added to the convective and viscous time-step constraints to facilitate explicit solution of the species equations. The chemical time-step constraint limited both relative and absolute changes in the species mass fractions. That is,

$$\Delta t_{\text{Chem}} = \min \left(\frac{\text{CFL}}{\lambda^{i}_{\text{Chem}}} \right) \tag{8}$$

where

$$\lambda^{i}_{\text{Chem}} = \frac{|\dot{w}_i + \delta_\varepsilon|}{\rho[\min(\delta_{\text{abs}}, \delta_{\text{rel}} Y_i) + \delta_\varepsilon]} \tag{9}$$

and where $\delta_\varepsilon = 1.E{-}6$, $\delta_{\text{abs}} = 1.E{-}2$, and $\delta_{\text{rel}} = 1.E{-}1$. CFL is Courant–Friedrichs–Lewy.

Definition of Efficiency

The mixing efficiency η_m for fuel lean conditions is the ratio of H_2 fuel that would react if complete combustion occurred to the total H_2 fuel injected. Two measures of chemical efficiency were employed. The first definition, $\eta_{c(H_2O)}$, is based on the amount of H_2O that is produced, and the second definition $\eta_{c(\Delta q)}$, is based upon the fraction of the chemical energy of the fuel that is released into the combustor. See Ref. 16 for details of the definitions of mixing and chemical efficiency.

Results and Discussion

The cases considered in this study are listed in Table 4. Figures 3 and 4 contrast the solutions obtained for laminar (case 2) and turbulent (case 3) nonreacting flow in the first half of the combustor. Figures 3 and 4 show contours of hydrogen mass fraction at crossflow planes at intervals of $0.5G$. The swept ramp and duct dimensions are outlined. The computational solution has been reflected about the z axis for visualization. The kidney-shaped structure of the jet plume remained compact and coherent in the laminar flow compared to the more diffuse jet plume observed in the turbulent flow. In addition to enhancing mixing between the jet and surrounding airstream, turbulence weakened the ramp generated vortex. The weakened vortex resulted in reduced jet penetration for turbulent flow. Differences in mixing between the calculated laminar and turbulent flowfields were significant, even in the near field of the injectors.

Table 4 Computational solutions

Case	ϕ	Turbulence treatment	Species and reactions	Domain and grid
1	0.0	Baldwin–Lomax	——	$x/G \leq 6.26$, $163 \times 39 \times 75$
2	0.7	Laminar	——	$x/G \leq 6.26$, $163 \times 39 \times 75$
3	0.7	Two-zone algebraic	——	$x/G \leq 6.26$, $163 \times 39 \times 75$
4	0.7	Two-zone algebraic	7, 7	$x/G \leq 6.26$, $163 \times 39 \times 75$
5	0.7	Two-zone algebraic	9, 19	$x/G \leq 6.26$, $163 \times 39 \times 75$
6	0.7	Two-zone algebraic	7, 7	$x/G \geq 6.26$, $77 \times 20 \times 75$
7	0.7	Two-zone algebraic	7, 7	$x/G \geq 6.26$, $77 \times 20 \times 101$

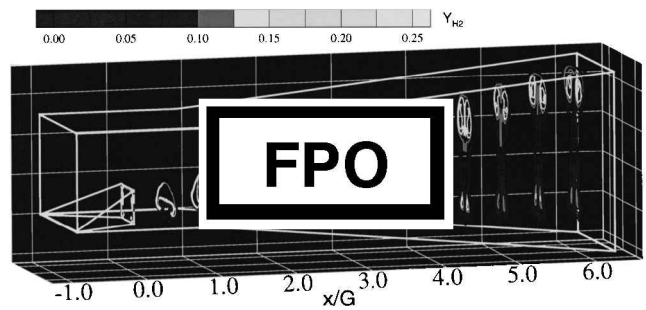

Fig. 3 Contours of hydrogen mass fraction for nonreacting laminar flow.

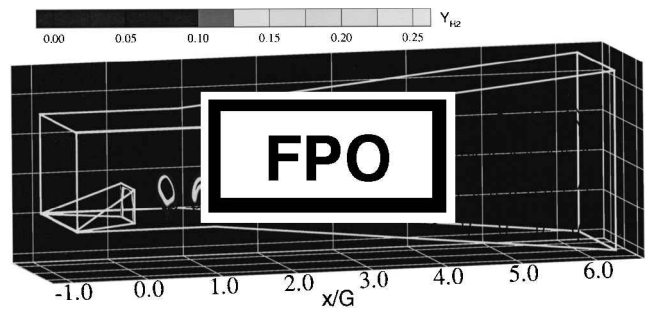

Fig. 4 Contours of hydrogen mass fraction for nonreacting turbulent flow.

Features of the turbulent, reacting flow in the first half of the combustor (case 4) are illustrated in Figs. 5 and 6. Figure 5 displays contours of hydroxyl mass fraction at crossflow planes at intervals of $0.5G$. Elevated levels of OH demarcate the reaction zone. The presence of OH in the exit plane of the injector ($x/G = 0.0$) illustrates that the reaction zone extended upstream of the injector. The reaction zone was found to roughly correspond to the stoichiometric surface. The equivalence ratio ϕ within the reaction zone was approximately $0.90 < \phi \leq 1.20$. The reaction zone at $x/G = 0.5$ was interrogated, and levels of OH mass fraction were found to exceed the equilibrium values by between 50 and 250%. The corresponding mass fraction of H_2O was found to be 10–15% less

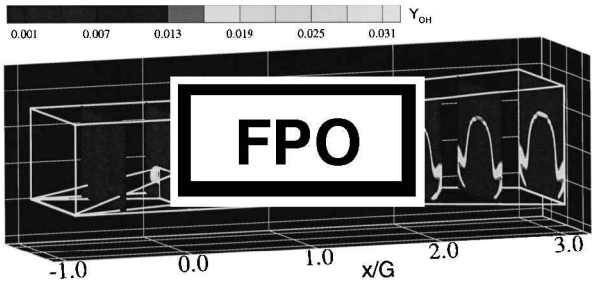

Fig. 5 Contours of OH mass fraction in the near field of the injector.

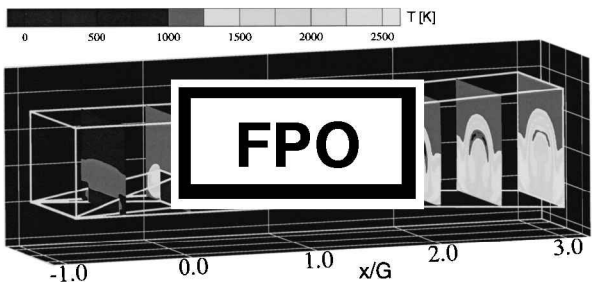

Fig. 6 Contours of temperature (K) in the near field of the injector.

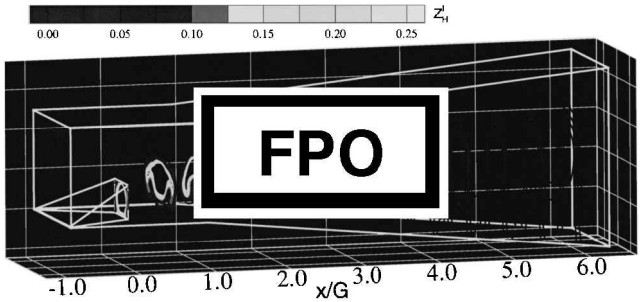

Fig. 7 Contours of injected elemental hydrogen for reacting flow.

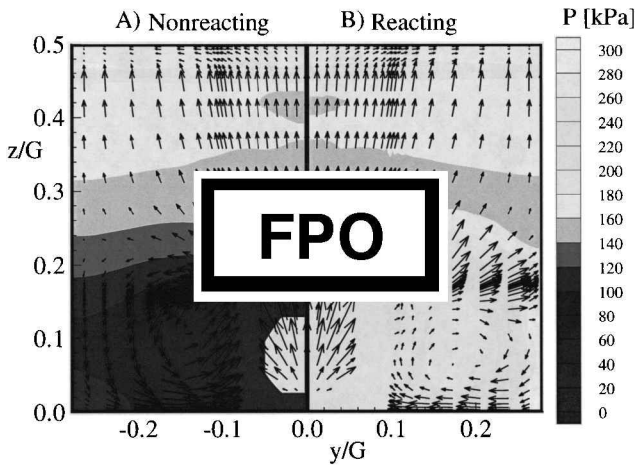

Fig. 8 Pressure contours (kPa) and velocity vectors at the exit plane of the ramp injector.

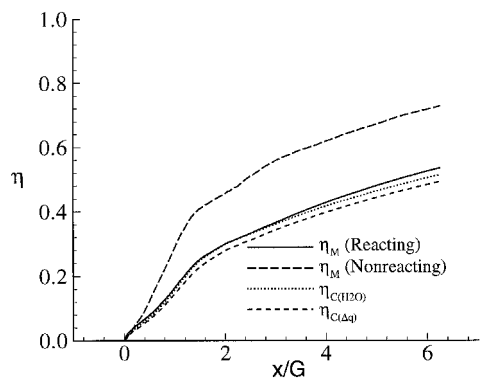

Fig. 9 Effect of reactions upon mixing and chemical efficiencies.

than its equilibrium value. On the fuel-rich side of the reaction zone ($\phi \geq 1.0$), the mass fraction of H_2O was found to be within 1% of its equilibrium value. Two counter-rotating vortices forced reacted products from the periphery of the jet plume into the center of the plume, which is most clearly observed at $x/G = 1.0$. The center of the jet plume was fuel rich, and the hydroxyl pulled into the plume by the action of the vortices decayed gradually downstream of $x/G = 1.0$. Figure 6 shows contours of temperatures at the respective crossflow planes. The oblique shock generated by the wedge increases the static temperature of the airstream along the jet centerline from 932 K to approximately 1060 K. The cold hydrogen jet (represented by the blue regions in Fig. 6) mixes with the airstream and reacts. The hot products from the reactions that were drawn into the center of the jet plume by the two vortices elevated the temperature within the center of the plume. The elevated temperatures within the plume also decayed downstream of $x/G = 1.0$, but not as rapidly as hydroxyl.

Chemical reactions were observed in the exit plane of the injector ($x/G = 0$). The onset of the reactions occurred at approximately $x/G = -0.16$. A strong streamwise recirculation zone was observed in the interstice region and extended downstream of the injector. The recirculation zone spanned the region $-0.20 \leq x/G \leq 0.85$. Velocities in the upstream direction in excess of 500 m/s were observed. At $x/G = 0.0$, the maximum velocity in the upstream direction was ≈350 ms. In contrast, the streamwise recirculation zone in the solution for nonreacting flow was limited to a small region in the base of the ramp.

Heat release dramatically reduced the mixing. Figure 7 shows contours of elemental hydrogen from the jet, Z'_H, at crossflow planes at intervals of $0.5G$. Z'_H is analagous to the hydrogen mass fraction for the nonreacting flows displayed in Figs. 3 and 4. It was obtained by subtracting the elemental hydrogen of the vitiated stream from the elemental hydrogen mass fraction. That is,

$$Z'_{\mathrm{H}} = Z_{\mathrm{H}} - c_{\mathrm{H}} \times Y_{\mathrm{N}_2} \tag{10}$$

where c_{H} is the ratio of elemental hydrogen to nitrogen by mass in the vitiated stream, Y_{N_2} is the mass fraction of nitrogen, and Z_{H} is the elemental mass fraction of hydrogen. The reduction in the mixing occurred primarily in the near field of the injector ($x/G \leq 2$). The reactions in addition to reducing the density, altered the flowfield surrounding the injector in two significant ways (Fig. 8). Every other vector at the exit plane of the injector along with contours of pressure is shown in the Fig. 8. First, the chemical reactions pressurized the near field of the injector so that the jet was nearly pressure matched rather than highly underexpanded in the case without reactions. Consequently, the initial expansion of the jet was reduced. Secondly, the streamwise vorticity as illustrated by the velocity vectors in the crossflow plane was reduced for the reacting case. The reduced vorticity resulted in reduced mixing. The reduction in streamwise vorticity as a result of heat release was observed by Riggins.[8] The effect of heat release in reducing mixing resulted in lower mixing efficiency values for the reacting flow compared to the nonreacting flow (Fig. 9). Figure 9 displays measures of chemical efficiency for the reacting flow. The two chemical efficiency curves lie close to the mixing efficiency curve; thus the flowfield was mixing-limited.

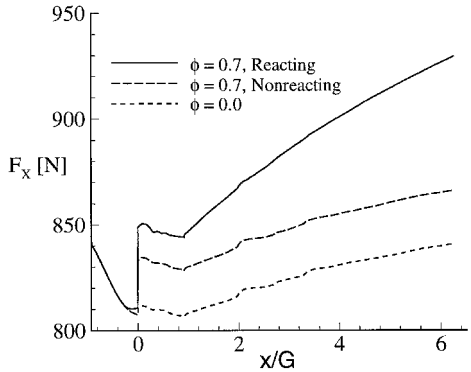

Fig. 10 Calculated integrated stream thrust.

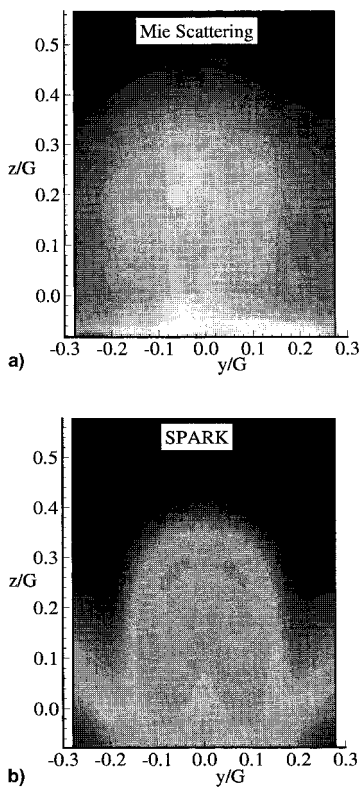

Fig. 11 Comparisons between a) Mie scattering image and b) calculated H_2O product mass fraction at $x/G = 3.0$.

The amount of OH, H, and O produced was relatively low compared with a previous study of the reacting flow from the normal injection of H_2 fuel into a Mach 2 vitiated airstream.[16] However, the flowfields in the previous study did not possess a large combustion-induced streamwise recirculation zone, which increased the residence time within the reaction zone.

Figure 10 shows the integrated stream thrust F_x, which for planes perpendicular to the x axis is simply

$$F_x = \int (p + \rho u^2)\, dA \tag{11}$$

The initial decrease in stream thrust ($x/G \leq 0.0$) reflected the drag generated by the inclined ramp. The small increase in F_x at $x/G = 0.0$ for the flowfield without injection (807–810 N) was because of the force exerted on the fluid by the back side of the ramp. The corresponding increases for the injection flowfields without reactions (807–833 N) and with reactions (810–849 N) reflected the increase in stream thrust caused by the momentum of the jet and the pressurizing of the back surface of the ramp for the reacting flow case. The loss in momentum because of friction is illustrated in the decrease in F_x for the constant area section of the duct ($0.0 \leq x/G \leq 0.9$). The pressure acting on the angled wall surfaces for $x/G > 0.9$ caused an increase in F_x. The increment in F_x between the two nonreacting flows remained relatively constant downstream of the injector. Heat release caused a gradual increase in stream thrust for the reacting flowfield relative to the nonreacting flows in the expanding region of the combustor.

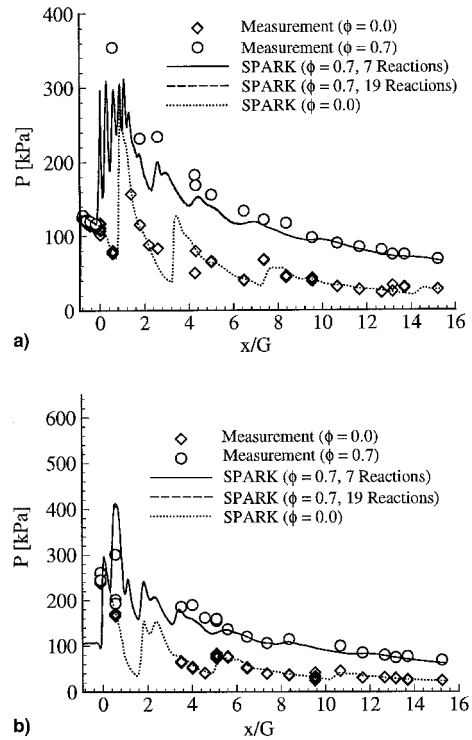

Fig. 12 Comparisons between the calculated and measured wall pressures (kPa) for the interstice centerline along the a) fuel injector wall and b) the opposite wall.

Comparisons between the experimentally measured data and the data from the Navier–Stokes calculations are displayed in Figs. 11–14. A Mie scattering image at $x/G = 3.0$, formed by averaging the images for the two interior ramps, along with the calculated H_2O product, is shown in Fig. 11. The calculated H_2O product mass fraction $Y^P_{H_2O}$ was obtained by subtracting the water of the vitiated stream from the water mass fraction. That is,

$$Y^P_{H_2O} = Y_{H_2O} - c_v \times Y_{N_2} \tag{12}$$

where c_v is the ratio of water to nitrogen by mass in the vitiated stream, and Y_{H_2O} is the mass fraction of water. The Mie scattering images are qualitative. However, the images indicated that the calculated penetration of the plumes of water product were in fair agreement with the penetration indicated by the Mie scattering images.

Figure 12 displays comparisons with measured wall pressures. Figure 12a shows comparisons along the fuel side of the interstice centerline. The agreement was excellent for the flowfield without injection ($\phi = 0.0$). The solution for the reacting flow exhibited a jagged pressure distribution along the interstice centerline in the near field of the injector. The upstream extent of the combustion-induced pressure rise agreed well with that observed in the measurements. The effect of including HO_2 and H_2O_2 was negligible. The pressure traces for the two solutions with the 7-species 7-reaction and the 9-species 19-reaction chemistry models were indistinguishable. The solution with the 7-reaction model was continued in the second half of the combustor, and excellent agreement was

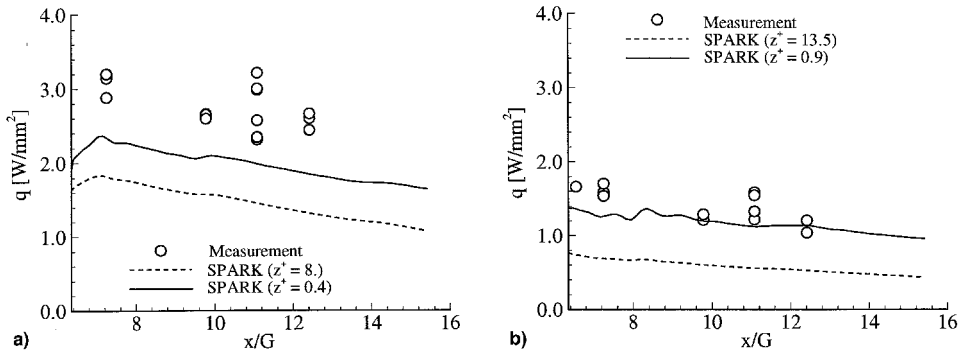

Fig. 13 Comparisons between the calculated and measured surface heat transfer (W/mm^2) for the interstice centerline along the a) fuel injector wall and b) the opposite wall.

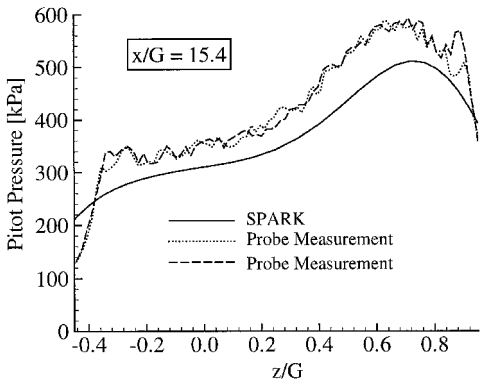

Fig. 14 Comparisons between the calculated and measured in-stream pitot pressures (kPa).

observed with the pressure measurements. Figure 12b shows comparisons along the opposite wall of the interstice centerline. Trends similar to those found along the fuel side were observed. The agreement was excellent for the no-fuel case. The calculated pressures were greater than the measured pressures at the first location downstream of the injector, x/G = 0.56. Again, the pressure traces for the solutions with the 7- and 19-reaction models were indistinguishable, and excellent agreement with the pressure measurements was observed in the second half of the combustor.

The calculated heat transfer obtained from the solution to the second half of the combustor is compared to heat transfer measurements in Fig. 13. Solutions were obtained on two computational grids. The heat transfer predictions on the fine grid were approximately 25% lower than the measured values on the fuel side of the interstice centerline, but the predictions from the fine grid solution were very close to the measurements on the opposite wall of the interstice centerline. The heat flux was greater on the fuel side of the wall, as expected. Finally, Fig. 14 shows a comparison of the calculated and measured pitot pressures along the interstice centerline at the exit of the combustor. The pitot pressures were lower on the fuel injector side of the combustor because of the decrease in total pressure associated with combustion. The combustion zone did not extend to the opposite wall, and this was reflected in the higher pitot pressures on the top wall. The comparison between the experimental and computational pitot profiles was encouraging. The maximum deviation was approximately 15%.

Summary and Conclusions

A computational study of a scramjet combustor with swept ramp fuel injectors was conducted with the SPARK Navier–Stokes computer code. Turbulence was modeled in the calculations with a two-zone algebraic turbulence model, while combustion was modeled with two finite rate H_2–air chemistry models.

The flowfield in the vicinity of the injector was found to be strongly affected by combustion. The mixing efficiency was observed to decrease by approximately 25% with combustion. In addition to decreasing the density, combustion was found to reduce the streamwise vorticity and pressurize the injector region so that the jet exhausted at nearly pressure-matched conditions. The reacting flowfield was mixing limited, and the combustion efficiency was within approximately 5% of the mixing efficiency.

Comparisons between the calculations and experimental measurements of the wall pressure, surface heat flux, in-stream pitot pressure, as well as Mie scattering flow visualization, indicated good overall agreement. The worst agreement for the wall pressures was in the immediate vicinity of the ramp injectors. Agreement with the instream pitot pressure measurements was particularly encouraging.

Acknowledgments

This work was supported under NASA Contracts NAS1-19320 and NAS1-19831. The authors thank Jeff White for his assistance in using his elliptic solver program for computational fluid dynamics grids. The use of the computing facilities at the Numerical Aerodynamic Simulation (NAS) Program is gratefully acknowledged.

References

[1]Mays, R. B., Thomas, R. H., and Schetz, J. A., "Low Angle Injection into a Supersonic Flow," AIAA Paper 89-2461, July 1989.

[2]Kraus, D. K., and Cutler, A. D., "Mixing Enhancement by the Use of Swirling Jets," AIAA Paper 93-3126, July 1993.

[3]Gutmark, E., Schadow, K. C., and Wilson, K. J., "Noncircular Jet Dynamics in Supersonic Combustion," *Journal of Propulsion and Power*, Vol. 5, No. 5, 1989, pp. 529–533.

[4]Haimovitch, Y., Gartenberg, E., Roberts, A. S., and Northam, G. B., "An Investigation of Wall Injectors for Supersonic Mixing Enhancement," AIAA Paper 94-2940, June 1994.

[5]Zaman, K. B. M. Q., Reeder, M. F., and Samimy, M., "Supersonic Jet Mixing Enhancement by Delta-Tabs," AIAA Paper 92-3548, July 1992.

[6]Menon, S, "Shock Waves for Enhanced Mixing in Scramjet Combustors," NASA CR-1028, Dec. 1989.

[7]Northam, G. B., Greenberg, I., Byington, C. S., and Capriotti, D. P., "Evaluation of Parallel Injector Configurations for Mach 2 Combustion," *Journal of Propulsion and Power*, Vol. 8, No. 2, 1992, pp. 491–499.

[8]Riggins, D. W., and McClinton, C. R., "A Computational Investigation of Flow Losses in a Supersonic Combustor," AIAA Paper 90-2093, July 1990.

[9]Waitz, I. A., Marble, F. E., and Zukosi, E. E., "A Systematic Experimental and Computational Investigation of a Class of Contoured Wall Injectors," AIAA Paper 92-0625, Jan. 1992.

[10]Davis, D. L., "Numerical Analysis of Techniques for Efficient Generation of Vorticity in Supersonic Flows," AIAA Paper 92-0828, Jan. 1992.

[11]Donohue, J. M., McDaniel, J. C., and Haj-Hariri, H., "Experimental and Numerical Study of Swept Ramp Injection into a Supersonic Flowfield," AIAA Paper 93-2445, June 1993.

[12]Stouffer, S. D., "The Effect of Flow Structure on the Combustion and Heat Transfer in a Scramjet Combustor," Ph.D. Dissertation, Virginia Polytechnic Inst. and State Univ., Blacksburg, VA, 1995.

[13]Eklund, D., and Stouffer, S., "A Numerical and Experimental Study of a Supersonic Combustor Employing Swept Ramp Fuel Injectors," AIAA Paper 94-2819, June 1994.

[14]Drummond, J. P., A Two-Dimensional Numerical Simulation of a Supersonic, Chemically Reacting Mixing Layer," NASA TM-4055, Dec. 1988.

[15]Carpenter, M. H., "Three Dimensional Computations of Cross-Flow Injection and Combustion in a Supersonic Flow," AIAA Paper 89-1870, June 1989.

[16]Eklund, D. R., and Northam, G. B., A Numerical Study of the Effects of Geometry on the Performance of a Supersonic Combustor," AIAA Paper 92-0624, Jan. 1992.

[17]Baldwin, B. S., and Lomax, H., "Thin Layer Approximation and Algebraic Model for Separated Turbulent Flows," AIAA Paper 78-257, Jan. 1978.

[18]Eggers, J. M., "Turbulent Mixing of Coaxial Compressible Hydrogen-Air Jets," NASA TN D-6487, Sept. 1971.

[19]Eklund, D., Fletcher, D., Hartfield, R., McDaniel, J., Northam, G., Dancey, C., and Wang, J., "A Computational/Experimental Investigation of Staged Injection into a Mach 2 Flow," *AIAA Journal*, Vol. 32, No. 5, 1994, pp. 907–916.

[20]Jachimowski, C. J., "An Analytical Study of the Hydrogen-Air Mechanism with Application to Scramjet Combustion," NASA TP 2791, Feb. 1988.

[21]Jachimowski, C. J., "An Analysis of Combustion Studies in Shock Expansion Tunnels and Reflected Shock Tunnels," NASA TP-3224, July 1992.

[22]Anderson, D. A., Tannehill, J. C., and Pletcher, R. H., *Computational Fluid Mechanics and Heat Transfer*, McGraw-Hill, New York, 1984, pp. 247–251.

[23]White, J. A., "Elliptic Grid Generation with Orthogonality and Spacing Control on an Arbitrary Number of Boundaries," AIAA Paper 90-1568, June 1990.